An effective thermal conductivity model for architected phase change material enhancer: theoretical and experimental investigations

Romain Hubert, Olivier Bou Matar, Jerome Foncin, Philippe Coquet, Dunlin Tan, Hongling Li, Edwin Hang Tong Teo, Thomas Merlet, Philippe Pernod

An Effective Thermal Conductivity Model For Architected Phase Change Material Enhancer : Theoretical and Experimental Investigations

Romain Hubert[a,b,c], Olivier Bou Matar[a], Jerome Foncin[b], Philippe Coquet[a,c], Dunlin Tan[c,d], Hongling Li[c], Edwin Hang Tong Teo[c], Thomas Merlet[b], Philippe Pernod[a]

[a] *Univ. Lille, CNRS, Centrale Lille, Yncrea Hauts-de-France, Univ. Polytechnique Hauts-de-France, UMR 8520 – IEMN, LIA LICS/LEMAC, F-59000 Lille, France*
[b] *Thales Land and Air Systems, 2 Avenue Gay Lussac, F-78990, France*
[c] *UMI 3288 CINTRA CNRS-NTU-THALES, Nanyang Technological University, Research Techno Plaza, 50 Nanyang Drive, 637553, Singapore*
[d] *Thales Research and Technology Singapore, 28 Changi North Rise, 498755, Singapore*

Abstract

Phase Change Materials (PCM) have been widely used for thermal energy storage due to their high latent heat of fusion. However, PCMs suffer from their very low thermal conductivity which limits heat spreading around the heat source. Without proper thermal conductivity enhancement, melting would occur mainly around the heat source and heat would be conducted too slowly for the device to be efficient. It is especially true when dealing with high power densities. Metallic foams are usually used as thermal conductivity enhancer, yet recent progress in additive manufacturing have allowed architected structures to be used and optimized. We present here an analytical investigation of the Effective Thermal Conductivity (ETC) of porous architected structures and emphasize is made on the effect of thermal constriction at the interface with a heat spreader in contact with the heat source. To confirm the efficiency of the model, it is compared to simulation data as well as experimental data obtained using flash laser method. Flash laser method data processing had to be modified to adapt to the porous media being characterized. For that purpose, a 1D finite difference model has been developed to solve the heat equation under flash laser conditions and derive the porous material effective properties. Using this model, architected structure were proven to have an ETC up to 75% higher than the one of foam for similar porosity in particular direction of space. The validity of the above mentioned model where proven through simulation, giving an almost perfect match and experiments detailed in this paper,which showed a maximum deviation of 11%.

Keywords: Effective thermal conductivity, Cellular materials, Homogenization, Phase change materials, Thermal constriction, Flash laser method

1. Introduction

PCM have become a main research topic lately because of their ability to store a relatively high amount of energy during phase change. Large numbers of PCM are available on the market with very wide melting and solidification temperature as well as different latent heat of fusion to better adapt to the very wide range of applications ranging from energy storage to thermal management. Despite their great energy storage ability, PCM suffer from their very low thermal conductivity which limits heat spreading around the heat source.

Several fillers are available to enhance their thermal conductivity [1], which can be divided into two different categories: *discrete* (carbon fibers, carbon nanotubes, nanoparticles) and *continuous* (metallic or carbon based foams, fins...). According to Ji *et al.* [1] continuous fillers outperform discrete ones because of the easier heat conduction in a continuous network. While discrete fillers can increase the PCM thermal conductivity by a factor 2, continuous fillers have been proven to reach an 18 times increase in thermal conductivity. Most continuous PCM enhancers used up to date are foams, which can suffer some drawbacks. Carbon-based foams allow the highest enhancement (18 times increase) but their manufacturing process limit their performances. They are actually made by Chemical Vapor Deposition [2] leading to a *patched* structure. At the interface of each patch phonon scattering occurs leading to a reduction of the thermal conductivity. It also makes the overall structure weaker from a mechanical point of view [3]. On the other hand while metal foams allow an 7 times increase (for copper foam), some features of their structure limit their thermal conductivity. While the foam is forming, matter tends to concentrate at the nodes, leading to hyperbolic profile struts [4; 5]. This creates additional thermal resistance at the center of the strut [6; 7; 8] where the cross sectional area is smaller. As the curvature of the profile increases, the ETC of the foam decreases. Finally, it has been showed that pore-size distribution follows a log-normal distribution, which standard deviation can influence foam ETC. Actually, using Voronoi tessellation, Baillis *et al.* [6] studied the effect of this parameter on the ETC and found out that as the standard deviation increased the ETC tended to decrease.

Engineered materials, whose properties and topology are tuned to achieve better than natural materials, are under rapid development due to the recent progress made in 3D-printing [9] that have allowed the manufacturing of complex nano and micro architectures. These materials have been widely used due to their outstanding combination of lightweight and mechanical properties especially in the aviation industry but also biomed-

Nomenclature

Abbreviations

CV	Control Volume
ETC	Effective Thermal Conductivity
PCM	Phase Change Material

Subscripts

f	Fluid
s	Solid
xy	*In-plane*
z	*Out-of-Plane*

Symbols

α_i	Node to Strut Cross Sectional Area Ratio
β	Pore size to strut radius ratio
ΔT	Temperature difference between the top and the bottom of the control volume (CV) (K)
ϵ	Porosity
η	Heat Spreader height to Strut Radius ratio
ω_i	Recalibration coefficient
ψ	Dimensionless Thermal Constriction Resistance
ρ	Density ($kg{\cdot}m^{-3}$)
θ, ϕ	Dimensionless Thermal Constriction decomposition terms
a	Gladwell Contact Spot Radius (m)
A_i	Cross Sectional Area (m^2)
b	Gladwell Cylinder Radius (m)
C_p	Specific Heat Capacity ($J{\cdot}kg^{-1}{\cdot}K^{-1}$)
e_i	Node height to Strut Length ratio
$G_{s,i}$	Dimensionless Thermal Resistance
h	Heat Spreader Height (m)
h_i	Convective Exchange Coefficients ($W{\cdot}m^{-2}{\cdot}K^{-1}$)
k_i	Thermal Conductivity ($W{\cdot}m^{-1}{\cdot}K^{-1}$)
L	Strut Length (m)
N	Number of Stacked Cells
P_s	Pore size (m)
Q	Heat flux ($W{\cdot}m^{-2}$)
R_c	Thermal Constriction Resistance ($K{\cdot}W^{-1}{\cdot}m^{-2}$)
s	Strut axis
t	Node height (m)

ical industry as scaffolds for tissue engineering as they have bone-like structure [10]. More recently, engineered or more generally cellular materials have been used because of their thermal properties although the literature regarding this subject remains scarce for now [11]. Depending on the intrinsic properties of the material they can be used as thermal insulator, thermal enhancer in heat storage unit or heat exchanger. In regard of the previous paragraph, the use of such engineered materials could lead to a better thermal conductivity as they have a perfectly periodic structure avoiding any of the effects previously mentioned. A large variety of periodic cellular material exists : lattice structures [12; 13; 14] , *shellular* materials [15; 16; 17; 18], hexagonal honeycomb, fins... Although, those periodic structures have been studied, no actual ETC model could be found in the literature [11] for them.

Due to their relative simplicity and freedom in term of topology tuning, lattice structures were selected. To have a better knowledge and optimize their topology to obtain the highest ETC as possible, mathematical model was needed. A large literature can be found on ETC modelling of foams, with the first one being Calmidi and Mahajan [19] model, which was developed using a 2D hexagonal honeycomb structure, which nodes (strut intersection) were represented as squares. This model was further developed and corrected successively by Bhattacharya *et al.*, [20], Boomsma and Poulikakos [21], Dai *et al.* [22] and finally Yang *et al.* [23; 24]. All achieved relatively good agreements with experimental measurements on foams [19; 25; 26], despite the wide variety of topology .

The first part of the following study aims at adapting for the first time the model developed by Yang *et al.* [23] for foams to several architected structure. It was chosen among others due to its relative simplicity and flexibility regarding the structure to be studied. Then, the model can be used to assess if the topology of architected structures can outperform the usual representation of the foam. The first part of the study dealt with isolated cell while actual structures infused with PCM are considered in the second part of the study. Those structures need to be packaged (i.e. surrounded by *walls*) to avoid any leaking. In addition, real case applications sometimes require the overall structure to only be a few cells thick which in terms of homogenization can cause issue as side effects may arise in these cases. Here thermal constriction has been shown to be the cause of side effects that are detrimental to ETC as heat flow is constricted when it enters the strut, which cross sectional area is smaller than other part of the device. Yang's model was combined to Gladwell's [27] to account for it. In the last part of the paper, the model previously described is validated using both simulation and experimental data. For that purpose a series of 12 different lattice structures were designed and the properties were derived using Flash laser method. Usual models [28; 29; 30; 31] used to derive thermal diffusivity require the material to be a mono-layer isotropic bulk, which is obviously not the case here. To over-

come it a 1D finite difference model was developed to solve the heat equation and derive the thermal conductivity of the samples through a least mean square algorithm.

2. Effective Thermal Conductivity model

Despite their great thermal or mechanical properties, cellular materials posses a complex structure, which leads, for large structures, to outstanding simulation computational cost. One way to overcome this issue is to use effective property model that would allow the representation of the material as a bulk. These model could also help optimizing the structure as they provide easier way to compare the efficiency of each topology. While it is admitted that both specific heat capacity and density can be calculated using mixing law, it has been proven to be wrong for thermal conductivity [25] and can be considered as an upper bound while the so-called parallel model is considered as a lower bound. A combination of those two models has been developed by Singh *et al.* [32] using a power model with a factor F which account for the fraction of struts oriented in the considered direction and which value is determined to fit experimental data. The difficulty to determine the value of F make this model hard to use in practice.

A different approach consists in considering a periodic structure that would statistically resemble foam and calculate the ETC on a cell of this structure. This was first done by Calmidi and Mahajan [19], who considered a hexagonal honeycomb which nodes (strut intersection) are represented as squares. It consists in slicing the cell perpendicular to the considered direction in layers on which the parallel model is applicable, once this is done the series model is used over the different slice to determine the ETC. This first model was corrected by Bhattacharya *et al.* [20] who replaced the square nodes by circular ones achieving better agreements with the experimental data provided by Calmidi and Mahajan on aluminum foams. Boomsma and Poulikakos [21] were the first to develop such model on a 3D geometry using a tetrakaidecahedron, which has been proven [33] among others structures [34; 35; 36] to be a good statistical representation of foam. It was corrected by Dai *et al.* [22] who identified mistakes in the calculations. The model was also extended to better estimate the node size, which is of major importance in the ETC calculation and whose calculation is hard to perform. In all papers previously mentioned this size is considered constant and its value is set so that the model would fit experimental data. The last correction and extension, to the author best knowledge, was realized by Yang *et al.* who change the mathematical formulation [23] while keeping the overall method identical and proposed a first expression of the dimensionless node size (normalized with the strut length) that is varying with porosity [24]. This avoids most of the geometrically impossible results caused by a constant dimensionless node size for high porosity foams. The expression of the dimensionless node size is given by a fourth degree polynomial expression derived through least mean square algorithm.

2.1. Lattice structure ETC

As mentioned in introduction, some foam features reflecting its randomness lead to a reduction of the effective thermal conductivity. It seems coherent to think that periodic structure with optimized topology would allow an ETC increase for a given porosity. To confirm this hypothesis four different lattices depicted on figure 1 are considered and their ETC is calculated using an adapted version of Yang *et al.* [23] model. The calculation of the FCC (figure 1b) cell ETC is depicted here. First, a heat flux (Q) is applied on the top surface (of area A_0) of the cell or CV, which is a cube having sides of length P_s. The effective material defined here has an effective thermal conductivity k_z in the vertical direction (referred to as *out-of-plan* direction) and k_{xy} in the plan normal to it (referred to as *in-plan* direction). The control volume is composed of a conductive solid material of thermal conductivity k_s and a fluid (PCM) of thermal conductivity k_f and of volume fraction ϵ. In that context the heat flux applied on the top surface create a temperature difference ΔT between the top and the bottom of the cell and can be expressed as [23]:

$$Q = k_z A_0 \frac{\Delta T}{P_s}. \tag{1}$$

The amount of heat transferred to the CV is conducted along the solid (Q_s) and the fluid (Q_f) phase in parallel [23], leading to :

$$Q = Q_s + Q_f. \tag{2}$$

Along the CV length the cross sectional area of the fluid phase stays almost constant due to the relatively large fluid volume ratio [23], called porosity, hence:

$$Q_f = k_f A_f \frac{\Delta T}{P_s}. \tag{3}$$

On the other hand, due to its complex geometry the cross sectional area of the solid phase varies along the CV, here a global expression of the heat flux over the entire cell cannot be guaranteed and a differential form along the strut axis s is preferred [23]:

$$Q_s = -k_s A_s(s) \frac{dT}{ds}. \tag{4}$$

Applying the separation of variables [23] method and integrating along the CV, yields:

$$Q_s = k_s \Delta T / \int_0^{P_s} \frac{1}{A_s(s)} ds. \tag{5}$$

Finally, eq. (1), (3) and (5) are substituted in eq. (2) leading to [23]:

$$k_z = k_s \left(\frac{P_s}{A_0}\right) / \left(\int_0^{P_s} \frac{1}{A_s(s)} ds\right) + k_f \epsilon. \tag{6}$$

For simplification purpose, eq. (6) is written as:

$$k_z = k_f \epsilon + k_s G_{s,z} (1 - \epsilon), \tag{7}$$

with :

$$G_{s,z} = \frac{1}{1-\epsilon} \frac{P_s}{A_0} / \left(\int_0^{P_s} \frac{1}{A_s(s)} ds\right). \tag{8}$$

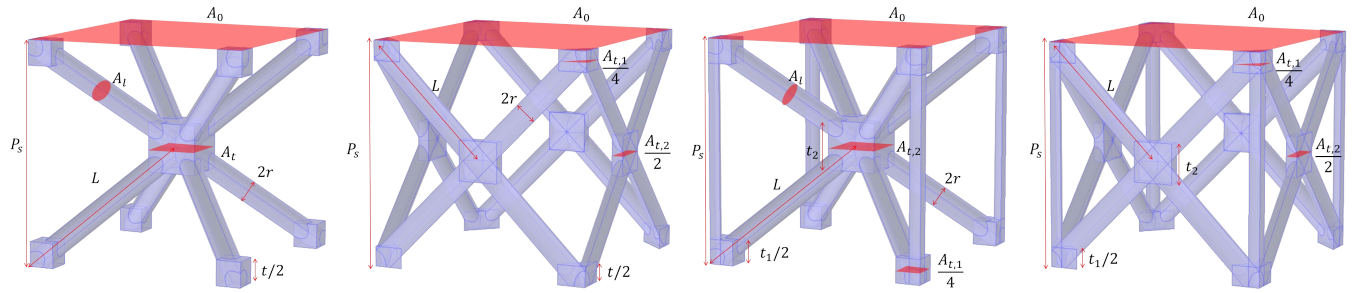

(a) (b) (c) (d)

Figure 1: Lattice cells and dimensions : (a) BCC, (b) FCC, (c) BCC_Z, (d) FCC_Z.

Here, $G_{s,z}$ (or later $G_{s,xy}$) is used as a way to simplify the expression of the ETC and highlighting the fact that a biased version of mixing law is needed to express it precisely. In addition, due to its expression $G_{s,z}$ could be seen as the dimensionless thermal resistance of a cell.

Two dimensionless parameters (α and e) are defined by Yang *et al.* [23] to relate node size (A_t, t) and strut size (A_l, L), where the A_i represents the feature's cross sectional area and t and L represents respectively the node's height and the idealized strut length:

$$\alpha = A_t/A_l,\ \alpha > 1, \tag{9}$$

$$e = t/L,\ e \geq 0. \tag{10}$$

In most cells (all except BCC) depicted on figure 1 two sets of parameters (α_1, e_1) and (α_2, e_2) are to be defined to account for the two kinds of nodes that are needed to precisely defined the structure:

To express the value of $G_{s,z}$ for the FCC structure, the porosity value is first expressed following the same calculation steps as the ones used by Yang *et al.* [23]: First the total volume (V_{tot}) of the cell is expressed as a function of L:

$$V_{tot} = P_s^3 = 2\sqrt{2}L^3. \tag{11}$$

Then, the total volume of solid (V_s) in this cell is determined:

$$V_s = 8 \times \left(L - \omega_\epsilon \frac{t_1 + t_2}{2}\right) + t_1 A_{t,1} + 2 \times t_2 A_{t,2}. \tag{12}$$

with ω_ϵ an additional constant term added to help accounting for complex interface between nodes and struts that make the actual strut and nodes lengths determination difficult. The porosity ϵ is defined as:

$$\epsilon = \frac{V_{tot} - V_s}{V_{tot}}. \tag{13}$$

Substituting equations 11 and 12 into equation 13 the following expression of the porosity is derived:

$$\epsilon = 1 - \frac{A_l}{L^2}\sqrt{2}\left(2\left(1 - \omega_\epsilon \frac{e_1 + e_2}{2}\right) + \frac{\alpha_1 e_1 + 2\alpha_2 e_2}{4}\right), \tag{14}$$

It will be determined later by fitting the ETC calculated by the model to the ones obtained by numerical simulations (see part 3). It can be noticed that two sets of parameter are needed for this particular topology. It can actually be seen on figure 1 that two different nodes exist: at the corner of the cell and in the center its sides. The value of those parameter will be evaluated in the next part.

The integral term that will be called dimensionless resistance is then calculated leading to:

$$\left(\frac{P_s}{A_0}\right) / \left(\int_0^{P_s} \frac{1}{A_s(s)} ds\right) = \frac{A_l}{L^2}\left[1 - \omega_z \frac{e_1 + e_2}{2} + 2\left(\frac{e_1}{\alpha_1} + \frac{e_2}{2\alpha_2}\right)\right]. \tag{15}$$

Here, ω_z and ω_{xy} are additional fitting parameters introduced to account for the complex strut to node interfaces and that will determined in part 3. From equations 8, 14 and 15 the global expression of $G_{s,z}$ i is derived:

$$G_{s,z} = \left(\left[2\left(1 - \omega_\epsilon \frac{e_1 + e_2}{2}\right) + \frac{\alpha_1 e_1 + 2\alpha_2 e_2}{4}\right] \times \left[1 - \omega_z \frac{e_1 + e_2}{2} + 2\left(\frac{e_1}{\alpha_1} + \frac{e_2}{2\alpha_2}\right)\right]\right)^{-1}. \tag{16}$$

In a similar way, $G_{s,xy}$ expression is established:

$$G_{s,xy} = \left(\left[2\left(1 - \omega_\epsilon \frac{e_1 + e_2}{2}\right) + \frac{\alpha_1 e_1 + 2\alpha_2 e_2}{4}\right] \times 2\left[1 - \omega_{xy} \frac{e_1 + e_2}{2} + \frac{e_1}{\alpha_1} + \frac{e_2}{\alpha_2}\right]\right)^{-1}. \tag{17}$$

Substitution of equation 16 or 17 in equation 7 allows the calculation of k_z and k_{xy} and finally the determination of the effective thermal conductivity tensor $\boldsymbol{K}_{eff}$:

$$\boldsymbol{K}_{eff} = \begin{pmatrix} k_{xy} & 0 & 0 \\ 0 & k_{xy} & 0 \\ 0 & 0 & k_z \end{pmatrix}. \tag{18}$$

The same process is repeated for the three other lattices depicted on figure 1 and the expressions of porosity and both $G_{s,z}$ and $G_{s,xy}$ are reported in tables 1 and 2 for those structures. The ones obtained for foam by Yang *et al.* [23] are also reported in tables 1 and 2 In table 2, $A_{2,z}$ and $A_{2,xy}$ refer respectively to the Out-of-plane and In-plane dimensionless thermal resistance while β refers to the pore size (P_s) to strut radius (r) ratio.

Type	Porosity (ϵ)	Dimensionless solid volume (A_1)
Foam [23]	$1-\frac{A_l}{L^2}A_1$	$3(1-e)+\frac{3}{2}\alpha e$
BCC	$1-\sqrt{3}\frac{A_l}{L^2}A_1$	$3(1-\omega_\epsilon e)+\frac{3}{4}\alpha e$
FCC	$1-\sqrt{2}\frac{A_l}{L^2}A_1$	$2(1-\omega_\epsilon\frac{e_1+e_2}{2})+\frac{e_1\alpha_1+2e_2\alpha_2}{4}$
BCC_z	$1-\sqrt{3}\frac{A_l}{L^2}A_1$	$3\left(1-\omega_\epsilon\frac{e_1+e_2}{2}\right)+\frac{\sqrt{3}}{4}+\frac{3}{8}(\alpha_2 e_2+e_1(\alpha_1-1))$
FCC_z	$1-\sqrt{2}\frac{A_l}{L^2}A_1$	$2\left(1-\omega_\epsilon\frac{e_1+e_2}{2}\right)+\frac{1}{2\sqrt{2}}+\frac{2\alpha_2 e_2+e_1(\alpha_1-1)}{4}$

Table 1: Structures porosity expression.

Type	$A_{2,z}$	$A_{2,xy}$	$G_{s,i}$
Foam [23]	$1-e+\frac{3e}{2\alpha}$	*Isotropic cell*	$\frac{1}{A_1A_{2,i}}$
BCC	$1-\omega_z e+\frac{4e}{\alpha}$	*Isotropic cell*	$\frac{1}{A_1A_{2,i}}$
FCC	$1-\omega_z\frac{e_1+e_2}{2}+2\left(\frac{e_1}{\alpha_1}+\frac{e_2}{2\alpha_2}\right)$	$2\left(1-\omega_{xy}\frac{e_1+e_2}{2}+\left(\frac{e_1}{\alpha_1}+\frac{e_2}{\alpha_2}\right)\right)$	$\frac{1}{A_1A_{2,i}}$
BCC_z	$2\frac{1-\omega_z(e_1+e_2)/2}{4+\sqrt{3}}+\frac{e_1(1+\alpha_2)+e_2\alpha_1}{\alpha_1(1+\alpha_2)}$	$2\left(\frac{1-\omega_{xy}(e_1+e_2)/2}{4}+\frac{e_2}{2\alpha_2}+\frac{2/\beta\sqrt{3}}{(2/\sqrt{3}-e_1)\beta\sqrt{3}/\pi^2+\alpha_1}+\frac{e_1-4/\sqrt{3}\beta}{2\alpha_1}\right)$	$\frac{1}{2A_1A_{2,i}}$
FCC_z	$2\frac{1-\omega_z(e_1+e_2)/2}{4+\sqrt{2}}+\frac{e_1(1+2\alpha_2)+e_2\alpha_1}{\alpha_1(1+2\alpha_2)}$	$2\left(\frac{1-\omega_{xy}(e_1+e_2)/2}{2}+\frac{e_2}{2\alpha_2}+\frac{\sqrt{2}/\beta}{(\sqrt{2}-e_1)\sqrt{2}\beta/\pi^2+\alpha_1}+\frac{e_1-2\sqrt{2}/\beta}{2\alpha_1}\right)$	$\frac{1}{2A_1A_{2,i}}$

Table 2: Structures $G_{s,z}$ and $G_{s,xy}$.

2.2. *Dimensionless parameters and constants determination*

As mentioned in the previous parts, determining the node size is of crucial importance to precisely estimate both porosity and effective thermal conductivity. The issue has been largely discussed, especially by Dai *et al.* [22] and Yang *et al.* [24]. The later insisted on the geometry impossibility linked to a biased estimation of the term e in Boomsma and Poulikakos [21] and Dai [22] model. Actually, Dai corrected Boomsma and Poulikakos model to better fit experimental data in part by changing e value but pointed out that both models could not avoid geometrical impossible results. Yang indicated that using Boomsma and Poulikakos or Dai expression of porosity for foam would lead to the following statement : as the porosity decreases, the ligament radius would increase while the length of the node remains constant to a point where the former exceeds the latter leading to impossible geometrical results. To improve the model Yang used a third degree polynomials which parameters were determined to better fit experimental results from Calmidi and Mahajan [19]. It is reported in table 3.

In the case of lattice structures, due to their regular and periodic geometry a more systematic method is used. Vaissier *et al.* [14] studied several lattice structures to be used as heat exchanger. To efficiently calculate both solid volume fraction and specific area (area per volume unit) Vaissier calculated the node volume and area of a variety of lattices and expressed it as a function of the strut diameter, which is known. Results from Vaissier *et al.* are used to determine the nodes volume of the structures depicted on figure 1 and derive the value of t_i and $A_{t,i}$ and infer e_i and α_i. Vaissier determined that the node volume is proportional to the cubic strut diameter and defined a proportionality ratio (γ_i), leading to:

$$A_{t,i}t_i = \gamma_i(2r)^3. \tag{19}$$

For a FCC structure, two nodes are identified, one type close the to cell corners and another in the middle of the side faces of the cell (see figure 1b). The nodes close to the corners are perfect cubes, which means that $A_t = t^2$. Using equation 19 and the fact that struts are considered perfect cylinder ($A_l = \pi r^2$) it leads to:

$$\alpha_1 = \frac{A_t}{A_l} = \frac{4}{\pi}\gamma_1^{2/3}, \tag{20}$$

combining equations 19 and 20, yields:

$$e_1 = \frac{t}{L} = \frac{\sqrt{2\pi\alpha_1}}{\beta}. \tag{21}$$

Equation 21 highlights the dependency of e on the evolution of β, the pore size to strut radius ratio. In the case of the second type of the node the calculations are different as this type of node is a cuboid meaning that $A_t = 2rt$ due to the arrangement of the struts at this particular point in the cell. This modifies the expression of α and e in this case, that are now given by:

$$\alpha_2 = \frac{A_t}{A_l} = \frac{4}{\pi}\gamma_2^{1/2}, \tag{22}$$

and

$$e_2 = \frac{t}{L} = \frac{\alpha_2\pi}{2\beta}. \tag{23}$$

The same operation is repeated for the other structures and the value of their respective α_i and e_i is reported in table 3. Finally, ω_z, ω_{xy} and ω_ϵ are determined. This is done using a gradient descent algorithm to fit simulation data (see figure 3). Their values are also reported in table 3.

2.3. *Numerical validation : Dimensionless constants calculation*

In order to validate the model described in the previous part and determine the dimensionless constants (i.e. ω_ϵ, ω_z and ω_{xy}) a set of simulation is run for the different structures on figure 1 using a commercial finite element software (COMSOL MULTIPHYSICS™). The simulation is run on a structure similar to the

Type	α_1	α_2	e_1	e_2	ω_ϵ	ω_z	ω_{xy}
Foam [23]	3/2	–	$327.26 - 1075.56\epsilon + 1182.83\epsilon^2 - 434.56\epsilon^3$	–	–	–	–
BCC	$\frac{4}{\pi}1.9933^{2/3}$	–	$\frac{2}{\beta}\sqrt{\frac{\pi\alpha_1}{3}}$	–	1.1269	2.3614	–
FCC	$\frac{4}{\pi}1.9933^{2/3}$	$\frac{4}{\pi}0.9041^{1/2}$	$\frac{\sqrt{2\pi\alpha_1}}{\beta}$	$\frac{\alpha_2\pi}{2\beta}$	1.2575	2.3451	2.1892
BCC$_z$	$\frac{4}{\pi}3.888^{2/3}$	$\frac{4}{\pi}1.9933^{2/3}$	$\frac{2}{\beta}\sqrt{\frac{\pi\alpha_1}{3}}$	$\frac{2}{\beta}\sqrt{\frac{\pi\alpha_2}{3}}$	1.0946	2.0033	1.9369
FCC$_z$	$\frac{4}{\pi}3.888^{2/3}$	$\frac{4}{\pi}0.9041^{1/2}$	$\frac{\sqrt{2\pi\alpha_1}}{\beta}$	$\frac{\alpha_2\pi}{2\beta}$	1.4044	1.5224	1.5059

Table 3: Dimensionless parameters expression and values.

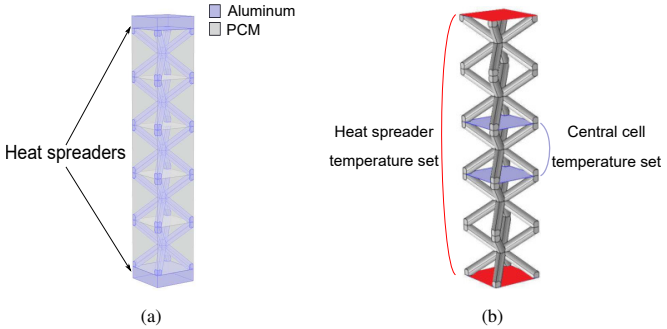

Figure 2: Pore-scale numerical simulation : (a) Pore scale modeling, (b) Temperature sets.

one depicted on figure 2 which is composed of five stacked-up BCC cells embedded between two plates called heat spreaders. These heat spreaders are added as they are a good representation of the *walls* that need to be added around the structure in real case applications to avoid any PCM leaking and to serve as a thermal interface between the heat source and the composite. To measure the ETC of a given structure, the heat equation is solved when the following boundary conditions are applied on the structure : a heat flux q is applied on the top surface of the top heat spreaders while a convective exchange condition is applied on the bottom surface of the bottom heat spreader. To be as close as possible of the condition of an isolated cell and avoid side effects as it is modeled in part 2 the ETC k_{cc} is measured on the central cell using :

$$k_{cc} = q\frac{P_s}{\Delta T_{cc}}, \tag{24}$$

with ΔT_{cc} the temperature difference between the top and the bottom of the central cell. The simulation is run for the four different topology described earlier and different porosity ranging from 0.55 to 0.99. We report the values of measured ETC on figure 3. On the same figure, the value of ETC calculated with the model of equation 7 re-calibrated to fit the simulation data are also reported showing good agreement.

Now, instead of using the temperatures measured on top and at the bottom of the central cell, a different set of temperature is considered : the difference between the temperature at the bottom of the top heat spreader and the one at the top of the bottom heat spreader, denoted ΔT_{cc}. This should give the ETC of

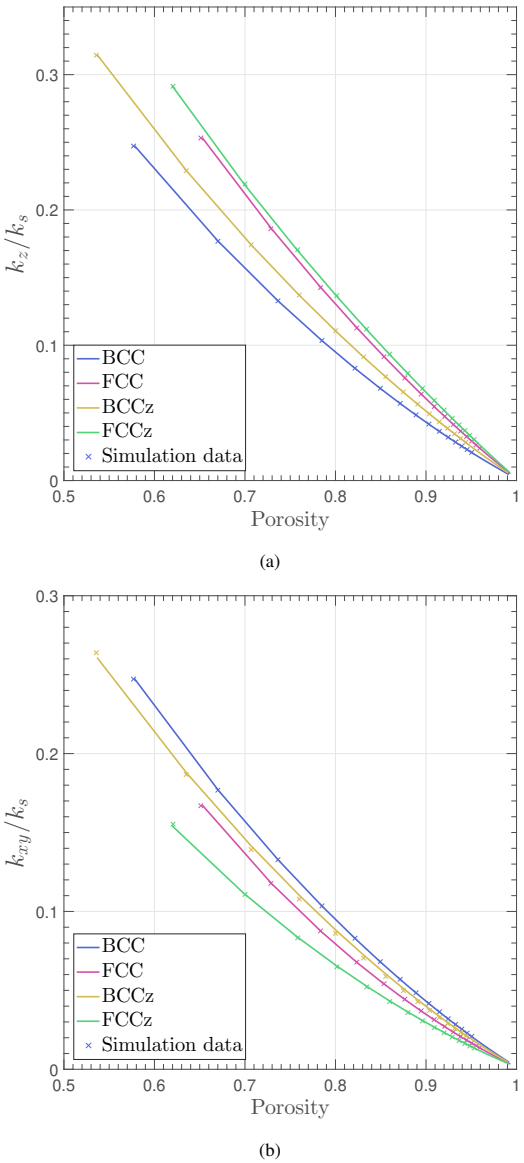

Figure 3: Normalized ETC validation:(a) k_z, (b) k_{xy}.

the entire structure using:

$$k_{hs} = q\frac{5P_s}{\Delta T_{ht}}, \tag{25}$$

Results obtained for a structure made of BCC cells of porosity 0.81 using both sets of temperature are compared for varying

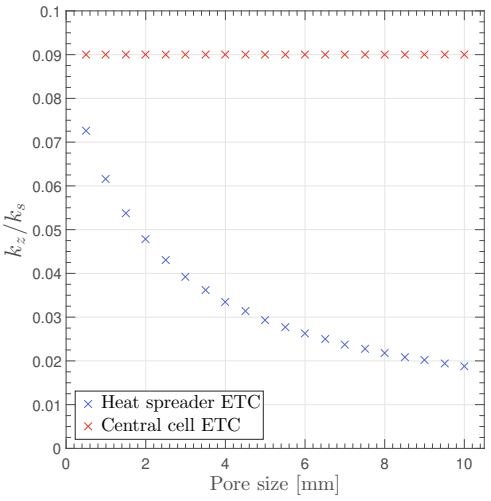

Figure 4: Comparison of the evolution of the ETC of a stack of BCC cell k_{hs} (in blue) and of the one of the central BCC cell k_{cc} (in red)showing the influence of thermal constriction at the interface between the composite and the heat spreaders.

pore size using equations 24 and 25 are depicted on figure 4. Unlike predicted by equation 7 a change of ETC for varying pore size and constant porosity is observed. In addition, k_{hs} seems to draw near k_{cc} when the pore size tends to zero. As seen in part 3, this is a consequence of side effects due to thermal constriction that will be implemented in the model later.

2.4. Discussion

Instead of directly comparing the ETC of the different structures for which Yang's model was adapted, to the foam, it would be more relevant to compare both $G_{s,z}$ and $G_{s,xy}$ respectively. Actually most of the ETC depends on the solid structure topology and material. Lattice's and foam's $G_{s,i}$ parameters are compared and data extracted from experimental measurement from Ranut [25], who performed an extensive review on foam ETC modeling and measurement as well as Yao [26] who performed himself measurements on copper foams, are added to illustrate Yang's model precision especially for copper foams. It should be noted that experimental data come from a very wide range of method, foam manufacturers and PCM which explain the deviation of Yang's model from the data.

$G_{s,z}$ and $G_{s,xy}$ values evolution with porosity are depicted on figures 5a and 5b both for foams, using Yang *et al.* [23; 24] and for architected structures using model in equations 5a and 17. On figure 5a an up-to 75% increase of $G_{s,z}$ is observed from foam to FCC_z structure while on figure 5b an up to 7% increase is noted. Both increases are linked to strut orientation and position both acting on the reduction or increase of the thermal path that the heat flow has to follow to go from one side of the cell to the other.

It should be noted that while Yang's model validity requires the porosity to be over 0.9, model presented in this paper has been proven to be valid for porosity as low as 0.55 through simulations, which results are shown on figure 3. This allows more

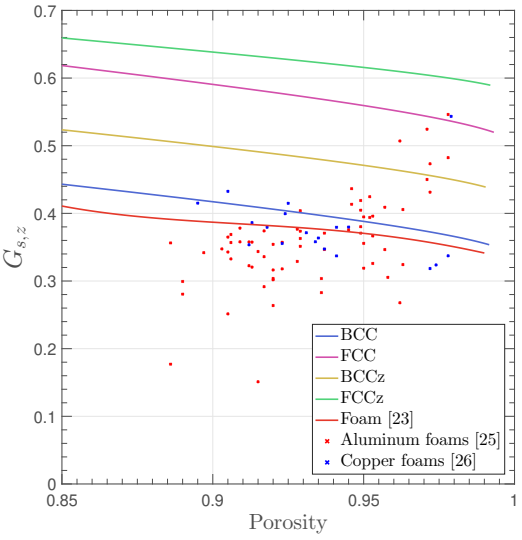

(a)

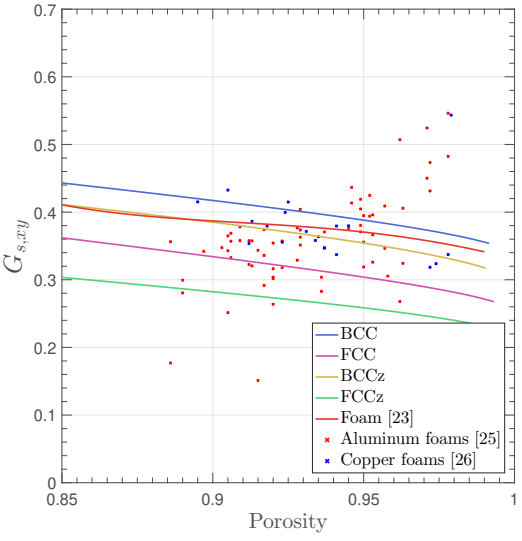

(b)

Figure 5: Topology parameters comparison:(a) $G_{s,z}$, (b) $G_{s,xy}$.

freedom in the design of the thermal management device to better adapt to tougher working conditions, especially *high* power density components requiring higher ETC to cope with higher heat flux.

The choice of one topology over the others may depend on several parameters : geometry of the system in relation with position of the heat source, manufacturing issues, thermal contact resistance between the composite and other part of the thermal management device (see part 3). For that reason it should be mentioned that, while FCC structure combine a relatively high out-of-plane ETC and a decent in-plane ETC, this is the lattice structure that requires the lowest β (pore size to strut radius ratio) to reach a certain level of porosity. This means that for a given pore size, this is the topology that necessitates the bigger strut radius. This is of relatively high importance when considering manufacturing. Actually, even if major progress has

been made in this field, limitations remain regarding the minimum strut radius that can be reached. This can cause issues when dealing with small size devices. In that sense, FCC would be considered here as the optimum topology.

3. Thermal constriction resistance

For mechanical purposes and to avoid any PCM leaking, the composite material formed by the PCM and an array of the selected cell need to be packaged. This is achieved by simply printing walls around the composite. Those walls have two purposes: avoid PCM from leaking and serve as thermal interface or heat spreader between the electronic component that is *cooled down* by the composite. At the interface between the so called heat spreader and the lattice cell a brutal change of cross sectional area is observed. Actually, if only one cell is considered, the heat flux was flowing in a solid of cross sectional area A_0 (see figure 1) but when it reaches the interface the section changes to be the one of the nodes $\alpha_1 A_l$. This brutal change causes additional thermal resistance due to a phenomenon called thermal constriction. These side effects reduce the composite ETC especially if the number of cells stacked in a given direction is reduced.

3.1. Thermal constriction modelling

Constriction phenomenon were first described to explain the additional electrical resistance occurring when two solids with relatively rough surfaces were put in contact [37]. At the interface, the real area of contact is not the one of the solids but the sum of a series of micro-contacts due to the roughness of both solids. This reduced contact area is the reason of the constriction : flux lines have a reduced path to go from one solid to another and *bend* to go through the micro-contacts. This is illustrated on figure 6, where heat flows between two solid having the same thermal conductivity k_s but having different width. If one wants to calculate the equivalent thermal resistance of such structure, the sum of the resistance of the

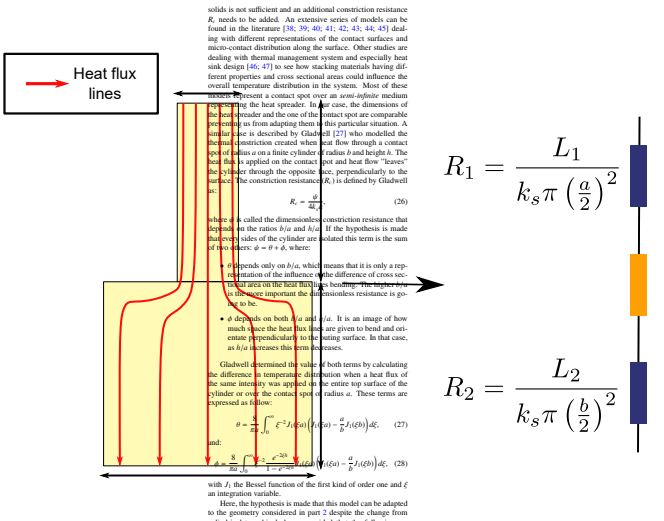

$$R_1 = \frac{L_1}{k_s \pi \left(\frac{a}{2}\right)^2}$$

$$R_2 = \frac{L_2}{k_s \pi \left(\frac{b}{2}\right)^2}$$

Figure 6: Additional constriction resistance at the perfect interface between two cylinders of very different cross sectional area

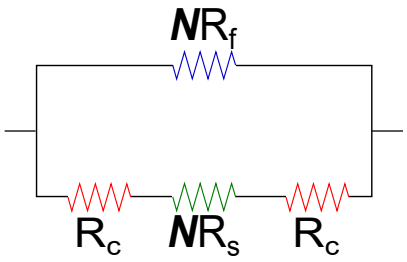

Figure 7: Thermal resistance network of the system constituted of a stack of N composite cells encapsulated between two heat spreaders.

- In the present case-study, the heat is flowing from the "opposite" surface to the contact spot. The change of direction of the heat flow has no influence on the constriction resistance.
- The change of shape has only small influence provided that the constriction resistance is calculated on a cylinder of height h and radius $\sqrt{A_0/\pi}$ with a contact spot of radius $\sqrt{\alpha_1 A_l/\pi}$, if heat spreaders are attached on top and at the bottom of the cell. This ensures conservation of cross sectional area for both heat spreader and contact spot.
- The PCM thermal conductivity is assumed to be small enough compared to the lattice structure material for the assumption of thermal insulation of the cylinder sides to be verified.

Now, instead of one, N FCC cells vertically stacked up on one another are considered, with one heat spreader attached at the top of the top cell and another at the bottom of the bottom cell (similar to figure 2a). Making the same assumption of parallel heat flow between the lattice structure and the PCM, the system can be represented as a thermal resistance network presented on figure 7 with:

$$R_s = \frac{P_s}{A_0 k_s G_{s,z}(1-\epsilon)}, \tag{29}$$

and

$$R_f = \frac{P_s}{A_0 k_f \epsilon}. \tag{30}$$

From this thermal resistance network, the new expression of the ETC accounting for side effects is determined:

$$k_z = k_s(1-\epsilon)G_{s,z}\left(1 + \frac{2R_c A_0 G_{s,z}(1-\epsilon)k_s}{P_s N}\right)^{-1} + k_f\epsilon. \tag{31}$$

In equation 31 appear clearly the influences of pore size and constriction resistance that have been considered negligible in most of the previous models. This can be explained by both device and foam structure : most of the devices found in the literature have characteristic sizes larger than a few pore size, which means that side effects have a minimum influence on the whole device. On the other hand there is usually no perfect contact between the composite and its packaging creating thermal resistance of a different nature.

3.2. Discussion

To assess the validity of the model in equation 31, a new set of simulation comparable to the one described in part 2.3. In that simulation set a unique FCC cell is modeled and its ETC is measured. Heat spreaders are attached on top and at the bottom of the cell. The simulation is run for four different porosity ranging from 0.85 to 0.98 and pore sizes ranging from $200\mu m$ to $3mm$ while the heat spreader thickness is $10\mu m$. Figure 8a depicts the computational domain for a cell size of 1000 µm having a porosity of 0.95. Figure 8b shows the mesh generated for such cell without displaying the PCM for clarity. Various grid resolutions are tested as seen on figure 9 which shows that a resolution of 1 000 000 is the resolution for which convergence is reached hence this resolution is chosen in the following simulations. The fact that ETC is measured on a unique cell with relatively thin heat spreaders should emphasise thermal constriction making it more visible. Figure 10 depicts the results of the the simulation and the comparison is made with both models in equations 7 and 31. Accounting only for topology (eq. 7) does not seem to be enough in that situation as constriction free model cannot fit simulation data, on the other hand the constriction model allows an almost perfect fit. Only a small deviation for *low* pore sizes mainly due to numerical limitations can be seen. It is interesting to see that as the pore size (and strut radius) decreases and becomes comparable to the heat spreader thickness the constriction model draws to the constriction free one, confirming the influence of both b/a and h/a. This study theoretically confirms the validity of the assumptions made in the previous part as well as the model itself. Nonetheless, it is important to note that ETC dependency of pore size is uniquely due to the presence of constriction.

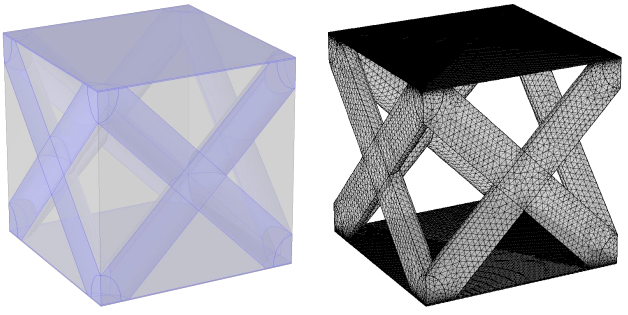

(a) (b)

Figure 8: Pore Scale Numerical Simulation on a FCC cell:(a) Computational Domain (Solid in blue, Fluid in grey), (b) Meshing of the architected structure, with PCM zone grid points omitted for clarity.

This model aims at making easier design and manufacturing of PCM architected thermal conductivity enhancers. It helps determine optimum cell topology as well as best surroundings to avoid a too strong influence of the side effects. Model depicted on equation 31 shows dependency of the ETC on five topological parameters that can be tuned using additive manufacturing:

- Cell general topology (BCC, FCC...),
- Porosity (ϵ),

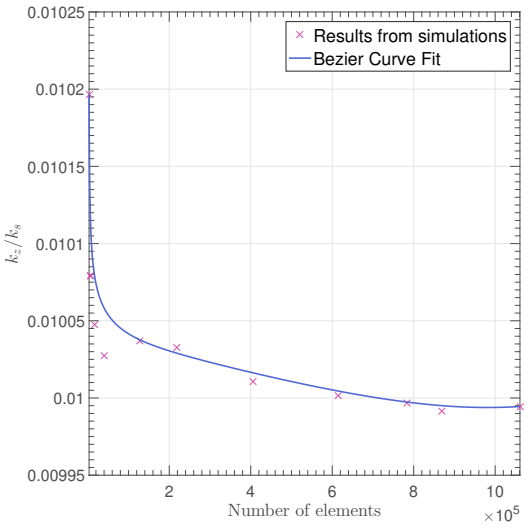

Figure 9: Mesh independency study of the pore-scale numerical simulation.

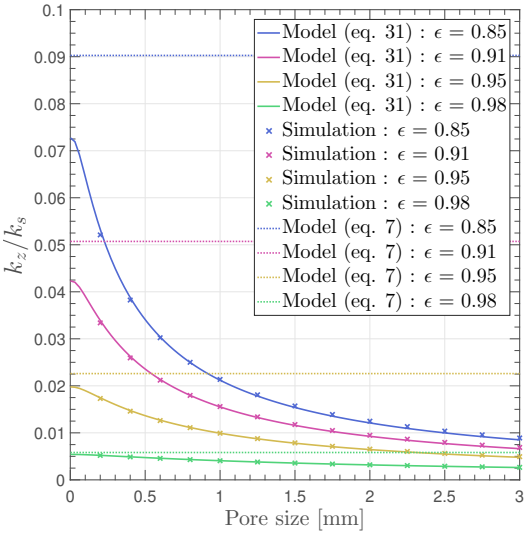

Figure 10: Thermal constriction model validation : Comparison of the normalized ETC calculated as a function of the pore size by finite element simulations (crosses), with model of equation 7 (dashed lines) and with the model of eq. 31 (continuous lines) for four different porosity (i.e. 0.85, 0.91, 0.95 and 0.98) of a FCC cell embedded between two 10µm thick heat spreaders

- Pore size (P_s),
- Heat spreader thickness (h),
- Number of stacked cell (N).

Figure 3 already depicted the influence of both cell topology and porosity on ETC. First, as FCC and FCC_z provide higher ETC it seems that orientation of the the struts closer to the heat flow direction is beneficial to the ETC. Actually, for both BCC and BCC_z structures, most struts have a higher angle from the heat flow direction, increasing the heat path from one side to the other side of the cell. It is interesting to observe that straight fins oriented in the heat flow direction would provide $G_{s,z} = 1$: in that case the law of mixture would be valid in that particular direction leading to a maximum ETC but the in-plane ETC would be drastically reduced in that case. On the other hand, one can observe that for all cell topology ETC increased with a decreasing porosity in a non-linear way unlike it is planned by law of mixture usually used to determined composite properties.

Sample	r	P_s	h	L	N	Type	ϵ
1	0.5	4	1	26	6	BCC	0.77
2	0.75	6	1	26	4	BCC	0.77
3	1	8	1	26	3	BCC	0.77
4	0.5	4	1	26	6	FCC	0.80
5	0.5	3	1	26	8	FCC	0.67
6	0.5	6	1	26	4	FCC	0.90
7	0.5	4	0.5	25	6	BCC_z	0.73
8	0.5	4	1	26	6	BCC_z	0.73
9	0.5	4	2	28	6	BCC_z	0.73
10	0.5	4	1	26	6	FCC_z	0.76
11	0.5	4	1	22	5	FCC_z	0.76
12	0.5	4	1	30	7	FCC_z	0.76

Table 4: Sample dimensions.

It was also proven that for a given porosity and heat spreader thickness, increasing pore size would be detrimental to the ETC (see figure 10). The same outcome is observe when decreasing the heat spreader thickness for a given porosity and pore size (see figure 11). Both statements are actually linked to the same phenomenon : thermal constriction is more dependent on those dimensions ratio than on their actual value which is clearly seen in equations 27 and 28. Actually, even if it is less practical in terms of manufacturing, describing structure by the value of $\beta = P_s/r$ and $\eta = h/r$ would give more information on their ability to conduct heat. This is visible on figure 11 where the dimensionless ETC is calculated as a function of the heat spreader thickness for 5 values of strut radius with fixed value of β.It appears that as long as the heat spreader thickness is superior to $r\sqrt{\alpha_1}$ (which corresponds to the node radius that is in contact with the heat spreader), the heat spreader thickness has almost no influence on the ETC.

Finally, when the number of cell in the heat flow direction increases, the value of both constriction resistances on top and at the bottom of the cell $2 \times R_c$ tends to become negligible compared to the total thermal resistance of the porous structure $N \times R_s$ as seen on figure 7.

4. Experimental validation

To validate the model presented in parts 2 and 3, ETC measurement were carried out by flash laser method on a series of samples presented in table 4 (all dimensions are given in *mm*) and figure 13. Those samples were design to validate the dependency of the ETC on four different parameters: porosity, pore size, heat spreader thickness and number of stacked cells with respect to the limitation of both flash laser method and additive manufacturing.

4.1. Experimental method

Flash laser method consists in sending an energy Dirac on one face of a cylindrical sample and recording the temperature evolution with time on the other side. A so-called thermogram is obtained and a series of models like the ones of Parker [28], Clark [29], Balageas [30] or Degiovanni [31] allow to derive the thermal diffusivity of the sample accounting eventually for radiative and/or convective loss on the sample sides assuming that samples respect three conditions : homogeneous, solid and isotropic. This technique possess several advantages: non-steady-state method allows for faster measurements as thermal processes usually take a long time to reach equilibrium. Fast method combined with low temperature increase limit heat loss during the measurement enhancing precision. The absence of contact with the heat source avoids any contact thermal resistance that usually lead to imprecision [28].

The first step of the experimental validation is the characterization of the base material. All samples are made by additive manufacturing using an *AS7* powder (aluminum alloy). Specific heat capacity is determined using a calorimeter while density is derived by precise weight and volume measurements. Flash laser method is used on bulky cylinder made in the same material and by the same process. The following properties are measured for this material at room temperature:

- $k_{Al} = 137\ W.m^{-1}.K^{-1}$ (Thermal conductivity)
- $C_p = 884\ J.kg^{-1}.K^{-1}$ (Specific heat capacity)
- $\rho_{Al} = 2542\ kg.m^{-3}$ (Density)

Flash laser method is then run on the samples described in table 4 but due to their specific topology, most models previously cited are unable to fit experimental thermograms which prevent any thermal diffusivity evaluation. Hence a different model is needed.

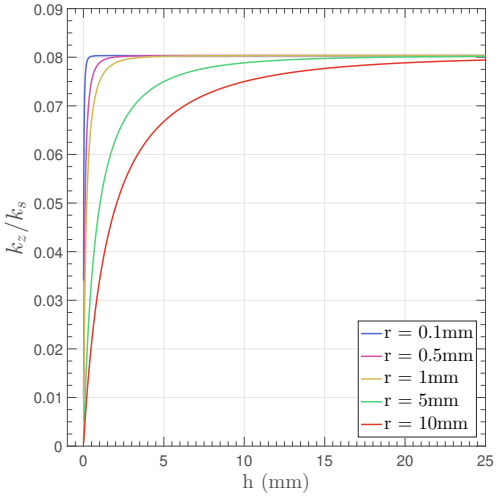

Figure 11: Heat spreader thickness influence: Comparison of the dimensionless ETC calculated using the model of eq. 31 as a function of the heat spreader thickness for 5 different strut radius of a FCC cell embedded between two heat spreaders

4.2. Experimental setup description

As explained earlier, flash laser method consists in applying a *Dirac* of energy on one face of the sample while measuring the temperature of the other side. Using one of the many existing models in the literature [28; 29; 48; 30], one is able to derive the thermal diffusivity of the studied sample for different experimental conditions that are accounted for through different boundary and initial conditions in the different models. Although any experimental conditions can be accounted for in the models, most of them include convective or radiative heat loss involving the estimation of convective or radiative exchange coefficient that are unknown for most materials. This motivates an experimental setup that avoid most heat loss. To do so, the sample is placed in a vacuum environment which reduce convective heat loss to the minimum, while radiative heat loss are reduced by the metallic enclosure the sample is placed in (see figure 12). This still leaves some ways for heat loss as the sample has to be placed on the setup, which creates heat loss by contact. Hence, the surface of contact between the sample and the setup is minimized as much as possible.

4.3. Experimental data processing

Samples described in table 4 do not respect any of the conditions necessary for the flash laser method models to be valid: they are heterogeneous, porous, anisotropic and have a diameter to height ratio that promotes heat loss on the sides. Actually, usual flash laser tailored samples have a very low length to radius ratio which is supposed to avoid most heat losses on the sides of the sample. A new model is required to be able to process experimental data accounting for all the above mentioned defects. Using usual model like Parker's [28] leads to poor fit with experimental data (see figure 15b and 15d). Those graphs depict the inability of usual models to predict precisely the temperature variation during the heating process (*first part* of the graph) and cannot account for any of the heat loss (*last part* of the graph). This is especially true for sample 3 that is composed of relatively big pores compared to other sample, which promotes complex heat flow. This does not ensure precise determination of the thermal diffusivity of the studied material. For that purpose, a 1D finite difference model is developed. In this model, samples are represented as a five layers material (see figure 14): two layers representing the top and bottom plates, one layer for the porous structure itself and two additional *interface* layers representing the half-filed pores that can be seen on figure 13 and 14. They were added for manufacturing reasons: they serve as a support for the plates to be printed. This method is similar to the one used in the determination of contact resistance using flash laser method [49; 50]. The properties of the different layers are denoted as:

- Heat spreader : k_{Al}, ρ_{Al} and C_p
- Lattice structure : k_{eff}, $\rho_{eff} = (1-\epsilon)\rho_{Al}$ and C_p
- Interface : $k_I = k_{eff} + k_{Al}/3$, $\rho_I = \rho_{Al}(1-\epsilon+1/3)$ and C_p

To determine the thermal conductivity of the interface, we consider a unit cell filled with two pyramids (at the top and at

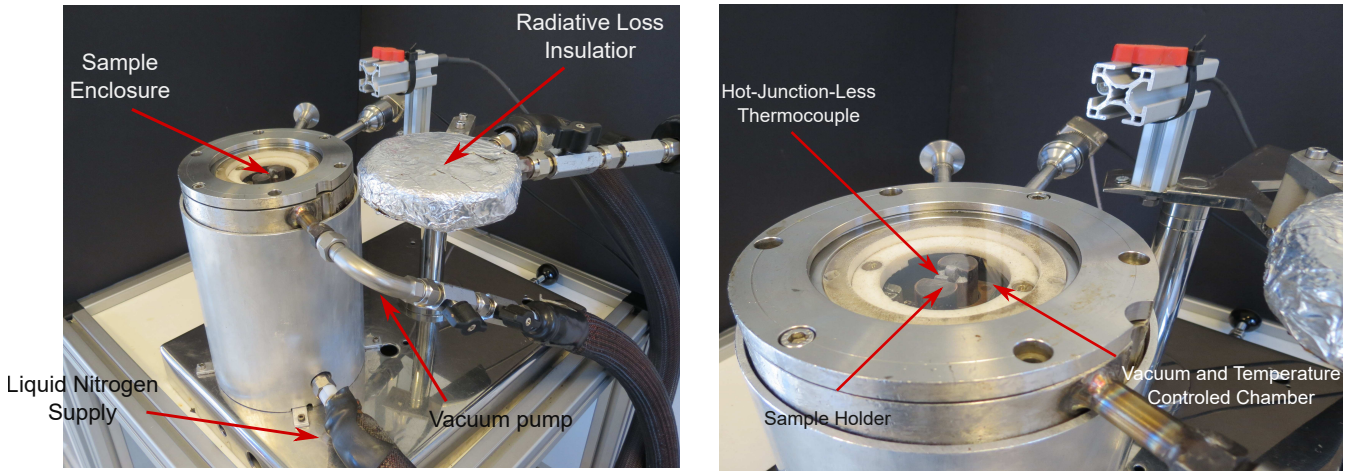

(a) (b)

Figure 12: Flash Laser Method Machine : (a) Global View, (b) Sample Chamber View.

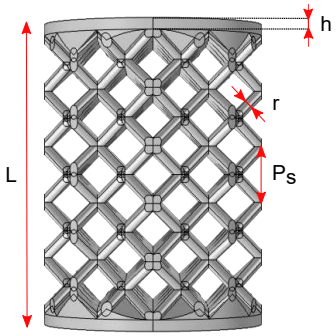

Figure 13: Sample scheme.

the bottom of it) representing a third of the cell volume. We then consider parallel heat flow between the struts and the pyramids. The mean cross section of the pyramid ($\bar{A}$) is defined, for a BCC structure, as :

$$\bar{A} = \frac{2}{P_s}\int_0^{P_s/2}(P_s - 2x)^2 dx = \frac{P_s^2}{3} = \frac{A_0}{3}, \tag{32}$$

similar results are obtained for other structures.

Considering parallel heat flow yields:

$$\frac{A_0 k_I}{P_s} = \frac{A_0 k_{eff}}{P_s} + \frac{\bar{A} k_{Al}}{P_s}, \tag{33}$$

leading to the expression defined above for the thermal conductivity of the interface.

Using this representation of the samples, the following heat equation is solved by a finite difference scheme:

$$\left.\frac{\partial T}{\partial t}\right|_{x,t} = \alpha(x)\left.\frac{\partial^2 T}{\partial x^2}\right|_{x,t} - \frac{2\pi h_r}{\pi R^2 k(x)}\left(T(x,t) - T_{ext}\right), \tag{34}$$

with x the position defined on figure 14, t the time and h_r a convective exchange coefficient with the outside environment at temperature T_{ext}. On top of the sample ($x = 0$), the following boundary condition (B.C.) accounting for the flash applied on the top surface is used:

$$-k(0)\left.\frac{\partial T}{\partial x}\right|_{0,t} = Q(t) - h_0\left(T(0,t) - T_{ext}\right), \tag{35}$$

with Q the heat flux due to the flash. It is time dependent as it is supposed to be short and h_0 is the convective exchange coefficient related to the top heat spreader. At the bottom of the sample, a simple convective exchange is considered leading to:

$$-k(L)\left.\frac{\partial T}{\partial x}\right|_{L,t} = h_L\left(T(L,t) - T_{ext}\right), \tag{36}$$

Between each layer, thermal resistance are added to better account for the variations of average properties induced by the different topology from one layer to another. Two thermal conductances are defined: h_b between the heat spreader and the interface and h_t between the interface and the lattice structure. The value of h_b is set relatively high compared to other conductance in the system. It actually represents the perfect contact between heat spreader and the base of the pyramids that are filling the pores close to it. Here, negligible thermal constriction is expected. On the other hand h_t is calculated using Cooper [38] model, who represented non-perfect contact of two solids by an array of cones in contact with each other. The expression was modified to account for the change of topology (from cone to pyramid). The coefficient $h_t$is defined as:

$$h_t = 4\left(\frac{1}{k_I} + \frac{1}{k_{eff}}\right)^{-1}\frac{2.2\sqrt{\alpha_2}r}{P_s^2}\left(1 - \frac{2.2\sqrt{\alpha_2}r}{P_s^2}\right)^{-3/2}. \tag{37}$$

The B.C at the different interfaces, separating each layers are now defined, starting with the one between the top heat spreader and the first interface material layer:

$$-k_{Al}\left.\frac{\partial T}{\partial x}\right|_{h^-,t} = h_b\left(T(h^+,t) - T(h^-,t)\right). \tag{38}$$

A similar B.C. is defined on the interface material side:

$$-k_I \left.\frac{\partial T}{\partial x}\right|_{h^+,t} = h_b \left(T(h^-,t) - T(h^+,t)\right). \quad (39)$$

The same set of equation is defined at the interface between the bottom heat spreader and the second interface zone. On the interface zone side the B.C. is defined as:

$$-k_I \left.\frac{\partial T}{\partial x}\right|_{(h+P_s/2)^-,t} = h_t \left(T((h+P_s/2)^+,t) - T((h+P_s/2)^-,t)\right). \quad (40)$$

while on the lattice structure side:

$$-k_{eff} \left.\frac{\partial T}{\partial x}\right|_{(h+P_s/2)^+,t} = h_t \left(T((h+P_s/2)^-,t) - T((h+P_s/2)^+,t)\right). \quad (41)$$

The model described here, is combined with a gradient descent algorithm to determine the value of thermal diffusivity of the lattice and interface layers as well as the exchange coefficients that lead to the best fit of the experimental thermograms. Results for sample 3 and 5 are depicted on figure 15a and 15c and show great improvements compared to Parker model (see figures 15b and 15d). For sample 3 residual has been greatly reduced while an almost perfect fit is obtained for sample 5. The difference of fitting quality can be explained by the structures of the two samples: samples 3 is composed of relatively large pore and have relatively high porosity compared to sample 5. This improvement in the experimental thermogram fitting provide a higher level of reliability in the thermal diffusivity and conductivity measurement, which was considered satisfying for all samples mentioned in table 4. Results are reported in table 5. Here, the values of thermal conductivity obtained using both models presented in equations 7 and 31 are compared to the experimental values to validate the global model and the effect of thermal constriction on actual structures.

4.4. Model validation

In table 5, experimental values from flash laser measurements are compared to the ones obtained using both models defined in equation 7 and 31. A maximum difference of 11.35%

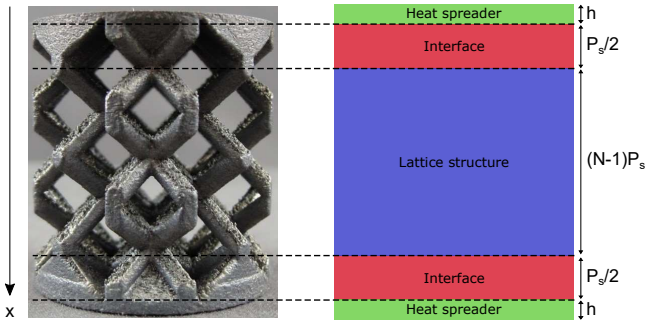

Figure 14: Sample 3 five layers model.

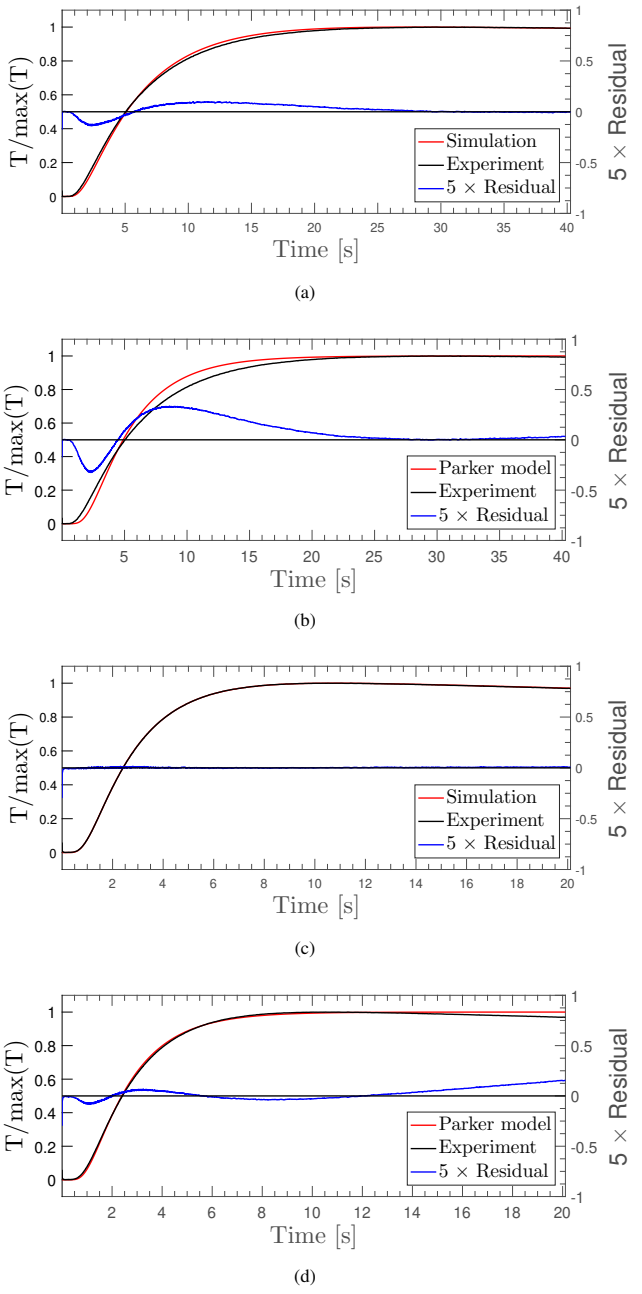

Figure 15: Model comparison for flash laser method thermogram fit : (a) Sample 3 fit using finite difference model, (b) Sample 3 fit using Parker model,(c) Sample 5 fit using finite difference model, (d) Sample 5 fit using Parker model

between models and experiment is observed for sample 5 which tends to validate the use of both model for ETC prediction of PCM architected enhancers.

Both models are compared for specific cases. Samples 1, 2 and 3 have been designed to see the influence of the pore size (4, 6 and 8mm) on the ETC. Obviously, model defined in equation 7 predicts an identical ETC for the three samples as it does not account for constriction while the contrary is true for the constriction model. When looking at the experimental values, a change is observed and is similar to the one predicted by the model though it is smaller than expected from sample 2

Sample	ETC Measured ($W.K^{-1}.m^{-1}$)	ETC Model ($W.K^{-1}.m^{-1}$)		Relative error (%)	
		Eq. 7	Eq. 31	Eq. 7	Eq. 31
1	16.86	18.00	17.18	6.75	1.86
2	16.34	18.00	16.61	10.18	1.66
3	16.22	18.00	15.92	10.96	1.90
4	19.66	19.34	18.39	1.60	6.43
5	37.48	34.58	33.22	7.72	11.35
6	8.85	8.55	8.03	3.36	9.27
7	23.56	23.68	22.25	0.50	5.56
8	22.83	23.68	22.66	3.70	0.77
9	23.48	23.68	22.78	0.84	3.00
10	22.58	23.17	22.19	2.60	1.73
11	22.41	23.17	22.01	3.39	1.80
12	23.21	23.17	22.33	0.15	3.79

Table 5: Sample ETC

to sample 3. This may be due to the presence of the pyramids that may reduce the effect of constriction increasing the space given to the heat flux lines to be constricted. In this case the validity of the constriction model is verified.

Samples 4, 5 and 6 were designed to observe the influence of porosity. In that case both models behave the same way than experimental values though constriction-free model gives better results. this might be explained by the slight difference between the model and the actual topology: struts tends to be larger than expected, this propagates to nodes topology changing how heat is transfer inside the sample. This is especially true for larger struts (i.e. smaller porosity). This effect is also combined to the one of pyramids that may also reduce the effect of constriction. Both models seems to be valid in that case as the effect of constriction is not clear. In this situation, constriction-free model gives better results here even though both models are within the error margin (around 10%).

The third set of samples is composed of samples 7, 8 and 9. Those have been designed to examine the consequence of a change of heat spreader thickness (0.5, 1 and 2mm). As mentioned before, if the heat spreader thickness is superior or *close* to the strut radius its influence on the ETC is negligible. Due to both manufacturing limitations and measurements requirements on sample dimensions, heat spreader thickness is of the same order of magnitude as the strut radius limiting its influence. Difference predicted by the constriction model is small. As a consequence experimental and model values do not follow the same trend and it is hard to conclude on the model validity from an experimental point of view. However both constriction and constriction-free predict ETC values close to the ones obtained experimentally.

A final set of samples composed of sample 10, 11 and 12 has been designed to corroborate the influence of the number of cells in the heat flow direction on the ETC. For the same reasons than the previous set the difference between each value is relatively small and may lie within the error margin. Even though experimental and model value fluctuate the same way it is hard to conclude on the validity on the constriction model from this experiment. However both models predict value close to the experimental ones.

To conclude, both models fit well experimental data as an average 4.1% difference is observed for constriction model (eq. 31) while an average 4.3% deviation is observed for the constriction-free model (eq. 7). Both deviations are within the error margin ensuring both model are valid. However, constriction model allows for refined ETC estimation as it predicts a variation of ETC for varying pore size (Sample 1 to 3). It could be argued that it fails to predict ETC variation in the case of varying heat spreader thickness or stacked-cell number but in those cases difference of ETC predicted by the model are so low that they might not be seen experimentally due to both defects inherent to additive manufacturing and experimental uncertainty.

5. Conclusion

An analytical model has been developed to assess the ETC of four different lattice structures (i.e. BCC, FCC, BCC_z and FCC_z). The ETC values for such structures are calculated and compared to the one obtained for foams using Yang *et al.* [23] model and showed an up-to 75% increase in ETC highlighting the potential of using architected structures over stochastic ones as PCM enhancers.

Assessing the validity of the above mentioned model (called constriction-free ETC model), more realistic structures were needed: stacked-up cells with so-called heat spreader on the top of the top cell and at the bottom of the bottom cell representing the possible PCM enclosure. Results from both simulations and experiments showed that thermal constriction appears at the interface between the heat spreaders and the architected structure itself. In that sens, additional parameters need to be accounted for to precisely assess the ETC, and another model (called constriction ETC model) accounting for thermal constriction was developed accounting for the influence of the following parameters:

- Cell topology : BCC, BCC_z, FCC and FCC_z,
- Porosity (ϵ),
- Pore size (P_s),
- Heat spreader thickness (h),
- Number of stacked up cell in the heat flow direction (N).

The validity of both model was assessed through simulations and experiments, using an adapted flash laser method (i.e. adapted to porous and anisotropic materials) which both showed good agreements. Actually the mean deviations for constriction and constriction-free ETC models were respectively 4.1 and 4.3% with a maximum deviation of respectively 11.35 and 10.96%. Both models could be considered equivalent when compared to experimental data but constriction ETC model can assess architected structure ETC in a more refined way in some specific cases and predict, for example, the variation of ETC for various pore sizes measured experimentally.

Acknowledgements

The authors are grateful to the financial support of Thales Land and Air System and the Agence Nationale Recherche Technologie (ANRT).

References

[1] H. Ji, D. P. Sellan, M. T. Pettes, X. Kong, J. Ji, L. Shi, and R. S. Ruoff, "Enhanced thermal conductivity of phase change materials with ultrathin-graphite foams for thermal energy storage," *Energy and Environmental Science*, vol. 7, no. 3, pp. 1185–1192, 2014.

[2] M. Loeblein, R. Y. Tay, S. H. Tsang, W. B. Ng, and E. H. T. Teo, "Configurable three-dimensional boron nitride-carbon architecture and its tunable electronic behavior with stable thermal performances," *Small*, vol. 10, no. 15, pp. 2992–2999, 2014.

[3] G. Zhang, *Thermal Transport in Carbon-Based Nanomaterials*, first edit ed., G. Zhang, Ed. Elsevier Inc., 2017.

[4] W. Y. Jang, A. M. Kraynik, and S. Kyriakides, "On the microstructure of open-cell foams and its effect on elastic properties," *International Journal of Solids and Structures*, vol. 45, no. 7-8, pp. 1845–1875, 2008.

[5] A. Liebscher and C. Redenbach, "Statistical analysis of the local strut thickness of open cell foams," *Image Analysis and Stereology*, vol. 32, no. 1, pp. 1–12, 2013.

[6] D. Baillis, R. Coquard, and S. Cunsolo, "Effective conductivity of Voronoi's closed- and open-cell foams: analytical laws and numerical results," *Journal of Materials Science*, vol. 52, no. 19, pp. 11 146–11 167, 2017.

[7] M. Bracconi, M. Ambrosetti, M. Maestri, G. Groppi, and E. Tronconi, "A fundamental analysis of the influence of the geometrical properties on the effective thermal conductivity of open-cell foams," *Chemical Engineering and Processing - Process Intensification*, vol. 129, no. March, pp. 181–189, 2018.

[8] J. Randrianalisoa, D. Baillis, C. L. Martin, and R. Dendievel, "Microstructure effects on thermal conductivity of open-cell foams generated from the Laguerre-Voronoï tessellation method," *International Journal of Thermal Sciences*, vol. 98, pp. 277–286, 2015.

[9] T. A. Schaedler and W. B. Carter, "Architected Cellular Materials," *Annual Review of Materials Research*, vol. 46, no. 1, pp. 187–210, 2016.

[10] H. Montazerian, E. Davoodi, M. Asadi-Eydivand, J. Kadkhodapour, and M. Solati-Hashjin, "Porous scaffold internal architecture design based on minimal surfaces: A compromise between permeability and elastic properties," *Materials and Design*, vol. 126, pp. 98–114, 2017. [Online]. Available: http://dx.doi.org/10.1016/j.matdes.2017.04.009

[11] I. Kaur and P. Singh, "Critical evaluation of additively manufactured metal lattices for viability in advanced heat exchangers," *International Journal of Heat and Mass Transfer*, vol. 168, p. 120858, 2021. [Online]. Available: https://doi.org/10.1016/j.ijheatmasstransfer.2020.120858

[12] K. N. Son, J. A. Weibel, V. Kumaresan, and S. V. Garimella, "Design of multifunctional lattice-frame materials for compact heat exchangers," *International Journal of Heat and Mass Transfer*, vol. 115, pp. 619–629, 2017.

[13] M. Leary, M. Mazur, J. Elambasseril, M. McMillan, T. Chirent, Y. Sun, M. Qian, M. Easton, and M. Brandt, "Selective laser melting (SLM) of AlSi12Mg lattice structures," *Materials and Design*, vol. 98, no. December, pp. 344–357, 2016.

[14] B. Vaissier, J.-P. Pernot, L. Chougrani, and P. Véron, "Computer-Aided Design Parametric design of graded truss lattice structures for enhanced," *Computer-Aided Design*, vol. 115, pp. 1–12, 2019. [Online]. Available: https://doi.org/10.1016/j.cad.2019.05.022

[15] A. Mirabolghasemi, A. H. Akbarzadeh, D. Rodrigue, and D. Therriault, "Thermal conductivity of architected cellular metamaterials," *Acta Materialia*, vol. 174, pp. 61–80, 2019. [Online]. Available: https://doi.org/10.1016/j.actamat.2019.04.061

[16] G. Park, S. Kang, H. Lee, and W. Choi, "Tunable multifunctional thermal metamaterials: Manipulation of local heat flux via assembly of unit-cell thermal shifters," *Scientific Reports*, vol. 7, no. January, pp. 1–15, 2017. [Online]. Available: http://dx.doi.org/10.1038/srep41000

[17] D. W. Abueidda, R. K. Abu Al-Rub, A. S. Dalaq, D. W. Lee, K. A. Khan, and I. Jasiuk, "Effective conductivities and elastic moduli of novel foams with triply periodic minimal surfaces," *Mechanics of Materials*, vol. 95, pp. 102–115, 2016. [Online]. Available: http://dx.doi.org/10.1016/j.mechmat.2016.01.004

[18] S. C. Han, J. W. Lee, and K. Kang, "A New Type of Low Density Material: Shellular," *Advanced Materials*, vol. 27, no. 37, pp. 5506–5511, 2015.

[19] V. V. Calmidi and R. L. Mahajan, "The Effective Thermal Conductivity of High Porosity Fibrous Metal Foams," *Journal of Heat Transfer*, vol. 121, no. 2, pp. 466–471, 1999.

[20] A. Bhattacharya, V. V. Calmidi, and R. L. Mahajan, "Thermophysical properties of high porosity metal foams," *International Journal of Heat and Mass Transfer*, vol. 45, no. 5, pp. 1017–1031, 2002.

[21] D. Poulikakos and K. Boomsma, "On the effective thermal conductivity of a three-dimensionally structured fluid-saturated metal foam," *International Journal of Heat and Mass Transfer*, vol. 44, no. 4, pp. 827–836, 2001.

[22] Z. Dai, K. Nawaz, Y. G. Park, J. Bock, and A. M. Jacobi, "Correcting and extending the Boomsma-Poulikakos effective thermal conductivity model for three-dimensional, fluid-saturated metal foams," *International Communications in Heat and Mass Transfer*, vol. 37, no. 6, pp. 575–580, 2010. [Online]. Available: http://dx.doi.org/10.1016/j.icheatmasstransfer.2010.01.015

[23] X. H. Yang, T. J. Bai, Jia XiLu, T. Kim, H. B. Yan, and J. J. Kuang, "An Analytical Unit Cell Model for the Effective Thermal Conductivity of High Porosity Open-Cell Metal Foams," *Transport in Porous Media*, vol. 102, no. 3, pp. 403–426, 2014.

[24] H. Yang, M. Zhao, Z. L. Gu, L. W. Jin, and J. C. Chai, "A further discussion on the effective thermal conductivity of metal foam: An improved model," *International Journal of Heat and Mass Transfer*, vol. 86, pp. 207–211, 2015.

[25] P. Ranut, "On the effective thermal conductivity of aluminum metal foams: Review and improvement of the available empirical and analytical models," *Applied Thermal Engineering*, vol. 101, no. 6, pp. 496–524, 2016. [Online]. Available: http://dx.doi.org/10.1016/j.applthermaleng.2015.09.094

[26] Y. Yao, H. Wu, and Z. Liu, "A new prediction model for the effective thermal conductivity of high porosity open-cell metal foams," *International Journal of Thermal Sciences*, vol. 97, pp. 56–67, 2015. [Online]. Available: http://dx.doi.org/10.1016/j.ijthermalsci.2015.06.008

[27] G. M. L. Gladwell and T. F. Lemczyk, "Thermal Constriction Resistance of a Contact on a Circular Cylinder with Mixed Convective Boundaries," *Proceedings of the Royal Society A: Mathematical, Physical and Engineering Sciences*, vol. 420, no. 1859, pp. 323–354, 1988.

[28] W. J. Parker, R. J. Jenkins, C. P. Butler, and G. L. Abbott, "Flash method of determining thermal diffusivity, heat capacity, and thermal conductivity," *Journal of Applied Physics*, vol. 32, no. 9, pp. 1679–1684, 1961. [Online]. Available: https://doi.org/10.1063/1.1728417

[29] L. M. Clark and R. E. Taylor, "Radiation loss in the flash method for thermal diffusivity," *Journal of Applied Physics*, vol. 46, no. 2, pp. 714–719, 1975.

[30] D. L. Balageas, "Nouvelle méthode d'interprétation des thermogrammes pour la détermination de la diffusivité thermique par la méthode impulsionnelle (méthode flash)," *Revue de Physique Appliquée*, vol. 17, no. 4, pp. 227–237, 1982.

[31] A. Degiovanni and M. Laurent, "Une nouvelle technique d'identification de la diffusivité thermique pour la méthode flash ," *Revue de Physique Appliquée*, vol. 21, no. 3, pp. 229–237, 1986.

[32] R. Singh and H. S. Kasana, "Computational aspects of effective thermal conductivity of highly porous metal foams," *Applied Thermal Engineering*, vol. 24, no. 13, pp. 1841–1849, 2004.

[33] W. Thomson, "On the Division of Space with Minimum Partitional Area," *Acta Mathematica*, vol. 11, pp. 121–134, 1887.

[34] E. B. Matzke, "The Three-Dimensional Shape of Bubbles in Foam-An Analysis of the Role of Surface Forces in Three-Dimensional Cell Shape Determination," *American Journal of Botany*, vol. 33, no. 1, pp. 58–80, 1946.

[35] D. Weaire and R. Phelan, "A counter-example to kelvin's conjecture on minimal surfaces," *Philosophical Magazine Letters*, pp. 107–110, 1994.

[36] R. Gabbrielli, "A new counter-example to Kelvin's conjecture on minimal surfaces," *Philosophical Magazine Letters*, vol. 89, no. 8, pp. 483–491, 2009.

[37] J. A. Greenwood, "Constriction resistance and the real area of contact," *British Journal of Applied Physics*, vol. 17, no. 12, pp. 1621–1632, 1966.
[38] M. G. Cooper, B. B. Mikic, and M. M. Yovanovich, "Thermal contact conductance," *International Journal of Heat and Mass Transfer*, vol. 12, no. 3, pp. 279–300, 1969.
[39] B. B. Mikic, "Thermal Contact Resistance," Ph.D. dissertation, Massachusetts Institute of Tecnology, 1966.
[40] B. B. Mikić, "Thermal contact conductance; theoretical considerations," *International Journal of Heat and Mass Transfer*, vol. 17, no. 2, pp. 205–214, 1974.
[41] K. K. Tio and K. C. Toh, "Thermal resistance of two solids in contact through a cylindrical joint," *International Journal of Heat and Mass Transfer*, vol. 41, no. 13, pp. 2013–2024, 1998.
[42] A. Degiovanni and X. Y. Zhang, "Modèle de résistances thermiques de contact entre deux surfaces cylindriques: Approche microscopique 3 D," *International Journal of Heat and Mass Transfer*, vol. 41, no. 3, pp. 601–612, 1998.
[43] A. Degiovanni, B. Remy, and S. Andre, "Thermal resistance of a multi-constrictions contact: A simple model," *International Journal of Heat and Mass Transfer*, vol. 46, no. 19, pp. 3727–3735, 2003.
[44] K. J. Negus, M. Yovanovich, and J. C. Thompson, "Constriction resistance of circular contacts on coated surfaces - Effect of boundary conditions," *Journal of Thermophysics and Heat Transfer*, vol. 2, no. 2, pp. 158–164, 2008.
[45] I. Argatov and I. Sevostianov, "On relations between geometries of microcontact clusters and their overall properties," *International Journal of Engineering Science*, vol. 47, no. 10, pp. 959–973, 2009. [Online]. Available: http://dx.doi.org/10.1016/j.ijengsci.2009.06.001
[46] P. Hui and H. S. Tan, "Temperature distributions in a heat dissipation system using a cylindrical diamond heat spreader on a copper heat sink," *Journal of Applied Physics*, vol. 75, no. 2, pp. 748–757, 1994. [Online]. Available: https://doi.org/10.1063/1.356480
[47] A. Desai, J. Geer, and B. Sammakia, "Models of Steady Heat Conduction in Multiple Cylindrical Domains," *Journal of Electronic Packaging*, vol. 128, no. 1, p. 10, 2006.
[48] A. Degiovanni, "Conductivité et diffusivité thermique des solides," *Techniques de l'ingénieur,Mesures physiques*, vol. 33, no. 0, p. 16, 1994. [Online]. Available: https://www.techniques-ingenieur.fr/base-documentaire/mesures-analyses-th1/mesure-des-grandeurs-thermophysiques-42544210/conductivite-et-diffusivite-thermique-des-solides-r2850/
[49] N. D. Milošević, M. Raynaud, and K. D. Maglić, "Estimation of thermal contact resistance between the materials of double-layer sample using the laser flash method," *Inverse Problems in Engineering*, vol. 10, no. 1, pp. 85–103, 2002.
[50] M. J. Colaço, C. J. S. Alves, and H. R. B. Orlande, "Transient non-intrusive method for estimating spatial thermal contact conductance by means of the reciprocity functional approach and the method of fundamental solutions," *Inverse Problems in Science and Engineering*, vol. 23, no. 4, pp. 688–717, 2015.

Graphical Abstract

An Effective Thermal Conductivity Model For Architected Phase Change Material Enhancer : Theoretical and Experimental Investigations

Romain Hubert, Olivier Bou Matar, Jerome Foncin, Philippe Coquet, Dunlin Tan, Hongling Li, Edwin Teo, Thomas Merlet, Philippe Pernod